Research Article | Vol. 32, No. 23 / 4 Nov 2024 / Optics Express 41892
Optics EXPRESS

Subwavelength-modulated silicon photonics for low-energy free-electron-photon interactions

OMER EMRE ATES, BENJAMIN J. SLAYTON, AND WILLIAM P. PUTNAM*

Department of Electrical and Computer Engineering, University of California, Davis, 1 Shields Avenue, Davis, CA 95616, USA
bputnam@ucdavis.edu

Abstract: We investigate silicon waveguides with subwavelength-scale modulation for applications in free-electron-photon interactions. The modulation enables velocity matching and efficient interactions between low-energy electrons and co-propagating photons. Specifically, we design a subwavelength-grating (SWG) waveguide for interactions between 23-keV free electrons and ≈1500-nm photons. The SWG waveguide and electron system exhibit a coupling coefficient of $|g_{Qu}| = 0.23$, and as we corroborate with time-domain, particle-in-cell simulations, the system operates as a backward-wave oscillator. Overall, our results show that modulated waveguides could open the door to strong, extended interactions between photons and low-energy (10-keV-scale) electrons, like those typically present in scanning electron microscopes. Additionally, our SWG waveguide design suggests that periodic waveguides could offer intriguing dispersion engineering opportunities for tailoring these interactions.

1. Introduction

The interaction of free electrons and photons in electron microscopes has recently attracted significant attention. In these interactions, electron beams are focused near structures supporting electromagnetic excitations, e.g., waveguides or nanoscale tips. As electrons pass these structures, they can coherently interact with the supported excitations and accelerate or decelerate, that is, they can absorb or emit photons. By measuring the electron energy spectra or the generated photons (or both) after the interaction, researchers have demonstrated novel microscopy modalities as well as unique opportunities for quantum technology. For example, such free-electron-photon interactions have been used in so-called photon-induced near-field electron microscopy (PINEM) to probe electromagnetic near fields around nanostructures at nm-scale spatial resolution [1,2] and with attosecond-level temporal resolution [3,4]. Furthermore, in the quantum realm, these interactions have been shown to enable correlation-enhanced imaging [5] and may support the generation of intriguing quantum states [6–10]. However, despite their promise for advanced microscopy and quantum science, these experiments have primarily been confined to large-scale, expensive transmission electron microscopes (TEMs).

TEM systems produce high-energy, typically >100-keV, electron beams that can enable strong free-electron-photon interactions. A strong interaction between a free electron and a photon requires two ingredients: a long interaction length and velocity matching, that is, the electron velocity should match the phase velocity of the interacting photon. As we will discuss further, when velocity-matched, the electron will experience a near constant electric field and can thereby exchange significant energy with the interacting electromagnetic wave. These two requirements can be achieved with high-energy electron beams (like those in TEM systems) and dielectric waveguides. For instance, an 120-keV electron has a velocity of $0.59c$, and common dielectric materials, like silicon nitride (refractive index ≈ 2), can readily be used to slow light to match this velocity. Indeed, researchers have recently demonstrated strong free-electron-photon interactions by velocity matching TEM-based, 120-keV electron beams to silicon nitride waveguides [5],

#537296 https://doi.org/10.1364/OE.537296
Journal © 2024 Received 23 Jul 2024; revised 18 Oct 2024; accepted 18 Oct 2024; published 1 Nov 2024

Optics EXPRESS

as well as by matching ≈200-keV beams to evanescent electromagnetic surface waves on glass interfaces [11,12].

Although high-energy electrons in TEM systems can support strong free-electron-photon interactions, low-energy electrons could provide new technological and scientific opportunities. First, on the technological side, scanning electron microscopes (SEMs) are an attractive platform for these interactions. In particular, in contrast to TEMs, SEMs offer large, easy-to-work-with interaction chambers, come at a comparatively low cost, and provide unique imaging capabilities. However, SEMs typically only support low-energy (10-keV-scale) electron beams; and, as we will discuss, it is challenging to design waveguides made of common dielectric materials that support modes with phase velocities matching such low electron energies. (We should note that free-electron-photon interactions have been demonstrated by passing SEM-based electron beams near optically-excited nanostructures [13]; however, these interactions, with only nm-scale interaction lengths, have remained relatively weak compared to their TEM-based counterparts.) Beyond technological opportunities, on the scientific side, recent work has shown that the free-electron-photon interaction strength might be maximized for low energy electrons [14]. Additionally, it has been demonstrated that very low energy (eV-scale) electrons might lead to intriguing new physical effects associated with recoil [15,16].

In this work, we aim to design structures to bring free-electron-photon interactions to the low-energy regime. Towards this end, we explore periodic dielectric waveguides to velocity match 10-keV-scale electrons to co-propagating photons over extended interaction lengths. We should mention that other researchers have recently begun to explore periodic waveguide structures for a similar purpose [17,18]. Here, we specifically look at periodic waveguides based on silicon photonics. We investigate these waveguides in the well-developed telecommunications band, at a free-space wavelength of ≈1500 nm, i.e., a frequency of ≈200 THz. As we will discuss, such periodic waveguides support slow spatial harmonics. These harmonics enable the coupling of slow, low-energy electrons to the guided photons, and our simulations indicate the possibility of achieving coupling coefficients with low-energy electrons comparable to those achieved with high-energy beams in TEM-based experiments.

The paper is organized into four sections. Following this introduction, in Section 2, we provide background information on the coupling of free electrons to modes of a waveguide. Next, in Section 3, we introduce the basics of periodic waveguides with subwavelength-scale modulation, and we analyze the coupling of an electron to the co-propagating modes of such a waveguide. In Section 4, we further our analysis by performing time-domain, particle-in-cell (PIC) simulations of our periodic waveguide. These simulations enable us to visualize the coupling and explore higher-order mode effects. Finally, we conclude with a brief summary of our results.

2. Background: free electrons coupling to uniform waveguides

The coupling of a free electron to a waveguide is illustrated in Fig. 1(a). In this work, we consider silicon waveguides on SiO_2 substrates, that is, silicon-on-insulator (SOI) waveguides. Additionally, throughout this work, we will use a coordinate system such that waveguide modes are confined in the xy-plane, and they propagate in the z-direction. In Fig. 1(a) and in this section, we consider a uniform waveguide; we call this waveguide uniform since it does not vary in the longitudinal z-direction. A cross section of the specific waveguide under consideration is shown in Fig. 1(b). The waveguide has a height of 250 nm and a width of 350 nm. The electron interacting with this waveguide travels in the z-direction above the waveguide at a height (that is, an impact parameter) of 50 nm. (This height is consistent with previous experimental results [5].)

Throughout this work, we investigate the electromagnetic characteristics of our waveguides numerically. Specifically, to analyze the basic modal properties of the waveguides, we use 2D modal analysis and 3D eigenfrequency simulations. (These simulations are performed in COMSOL.) For the uniform waveguide, since there is no variation in the z-direction, 2D modal

Optics EXPRESS

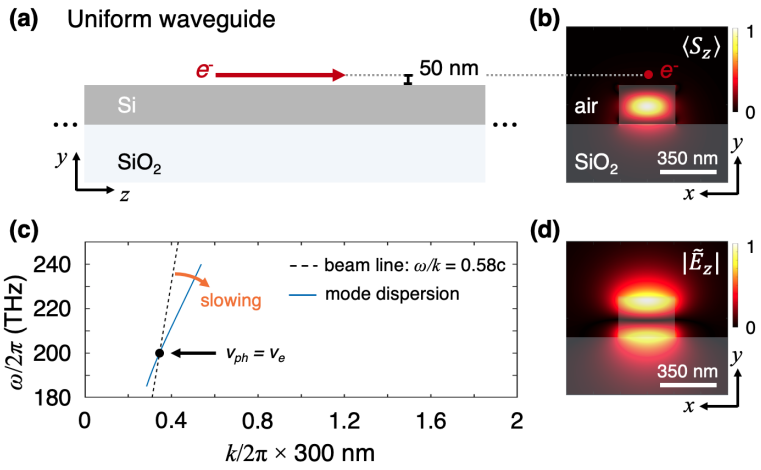

Fig. 1. Free-electron-photon coupling with a uniform waveguide. (a) Illustration (side view) of the waveguide with the propagating free electron. (b) The time-average Poynting vector in the z-direction (i.e., the intensity) of the fundamental TM-like mode in the waveguide (normalized). (c) Dispersion diagram showing that at 200 THz (1500-nm wavelength) the fundamental TM-like mode in the designed uniform waveguide velocity matches with 116-keV free electrons ($v_e = 0.58c$). (The waveguide cross-section has been selected to put the frequency of interest, 200 THz, near cutoff.) (d) Longitudinal (z-directed) electric field distribution of the fundamental TM-like mode (normalized).

analysis is sufficient. This solver returns the complex field amplitudes and propagation constants for a given frequency. Accordingly, mode profiles, dispersion, and (as we will discuss) coupling strength can be readily computed. For instance, in Fig. 1(b), we show the intensity profile of the fundamental TM-like mode of our uniform waveguide; and in Fig. 1(d), we show the magnitude of the z-directed electric field of this mode. Both of these plots correspond to a frequency of 200 THz, that is, a free-space wavelength of 1500 nm.

The interaction of an electron with a waveguide mode is controlled by the longitudinal, z-directed electric field. For a strong interaction between the electron and the mode, the electron must experience a strong electric field in its direction of propagation. As illustrated in Fig. 1(d), the fundamental TM-like mode possesses a strong z-directed electric field above the waveguide at the position of the electron [19]. Therefore, in this work, we will primarily focus on the fundamental TM-like mode.

Beyond a strong z-directed field, a strong electron-mode interaction requires *velocity matching*. For a strong interaction, we want the electron to experience a near-constant electric field. A constant field can consistently accelerate (or decelerate) the electron and can thereby enable a significant energy exchange between the electron and the mode. To achieve such a constant field, we require the electron velocity, v_e, to match the phase velocity of the interacting mode, v_{ph}. Velocity matching can be visualized on a dispersion diagram, as illustrated in Fig. 1(c). In Fig. 1(c), we show the dispersion of the fundamental TM-like mode of our uniform waveguide from 185 to 240 THz. (The cutoff frequency is 180 THz.) Overlapping the dispersion, we include a beam line; the beam line corresponds to all points in ω-k space with phase velocity equal to v_e. Therefore, the intersection of this beam line with the dispersion curve of our mode indicates a velocity-matching point, where $v_e = v_{ph}$. In Fig. 1(c), the beam line corresponds to an electron velocity of $0.58c$ or an electron energy of $E_e = 116$ keV. This electron velocity matches the phase velocity of our mode at the frequency of interest, 200 THz. Lastly, we should also note that

Optics EXPRESS

slowing down the electron corresponds to changing the slope of our beam line, as indicated in Fig. 1(c).

To quantify the strength of the electron-mode interaction, we use the standard coupling coefficient, g_{Qu}. The coupling coefficient is defined in Ref. [6], and can be written as:

$$g_{\mathrm{Qu}} = \frac{e}{2\hbar\omega\sqrt{n_{\mathrm{ph}}}} \int_0^{L_{\mathrm{int}}} \tilde{E}_z(z') e^{j\omega z'/v_e} dz', \tag{1}$$

where $\tilde{E}_z$ is the z-directed electric field (in phasor form) of the waveguide mode at frequency ω and at the beam position; L_{int} is the interaction length between the electron and the mode; and n_{ph} is the average number of photons in the waveguide (over the length L_{int}). The average number of photons in the waveguide is equal to the total time-average electromagnetic energy in the waveguide (over the length L_{int}) divided by the photon energy (that is, $\hbar\omega$). We should additionally note that for the waveguides considered here this time-average electromagnetic energy is proportional to the peak value of $|\tilde{E}_z|^2$ as well as L_{int}. Lastly, to define our conventions, we should note that the real, z-directed electric field in our formulation is given by $E_z(x, y, z, t) = \mathrm{Re}\{\tilde{E}_z(x, y, z)e^{j\omega t}\}$.

The expression for g_{Qu} can be understood intuitively by considering it in two parts. First, the integral in g_{Qu} can be seen to be L_{int} multiplied by the average, z-directed electric field that an electron moving at velocity v_e experiences when traveling near the waveguide mode at frequency ω. Second, the term preceding the integral acts as a normalization term. So, g_{Qu} gives us an idea of the average, normalized, z-directed electric field experienced by the interacting electron. With this understanding, we see that with velocity matching, we expect a large average field and, thereby, a large g_{Qu}. Lastly, to provide a more concrete physical meaning of g_{Qu}, we should mention that it has been argued that $|g_{\mathrm{Qu}}|^2$ is equal to the expected number of photons produced by a single electron interacting with the specified mode [6]. (More specifically, a single electron is expected to produce a coherent state with an average number of photons given by $|g_{\mathrm{Qu}}|^2$ [6].)

In Fig. 2, we plot the coupling coefficient for the interaction of an electron with the fundamental TM-like mode of the uniform waveguide presented in Fig. 1. Specifically, we plot $|g_{\mathrm{Qu}}|$ versus the (experimentally relevant) electron velocity and frequency of the mode. Looking at the results, we see that high values of $|g_{\mathrm{Qu}}|$ map out a curve. This curve corresponds directly to the dispersion of the mode: given a specific frequency ω, the point of high $|g_{\mathrm{Qu}}|$ corresponds to the electron velocity where the beam line intersects the dispersion curve at ω (that is, the velocity-matching point). For instance, the intersection shown in Fig. 1(c) is labeled with the black dot in Fig. 2. Additionally, the orange arrow in Fig. 2 indicates the movement along the dispersion curve associated with slowing the electron velocity (as also indicated in Fig. 1(c)). In the right panel of Fig. 2, we also plot $|g_{\mathrm{Qu}}|$ along the vertical line passing through the black dot (that is, we plot $|g_{\mathrm{Qu}}|$ at varying electron velocities at a frequency of 200 THz). We see that $|g_{\mathrm{Qu}}|$ exhibits sinc-like oscillations, as expected from the nature of the phase-matching integral in the definition for g_{Qu} [20].

From the results in Fig. 2, we can extract several important lessons about the interaction between an electron and a waveguide mode. First, the coupling should be stronger at frequencies closer to the cutoff frequency. This has been previously observed [21] and is intuitive: near cutoff, more of the mode is pushed out of the high-index core of the waveguide. Therefore, the electric field at the position of the electron is greater. For example, the black dot in Fig. 2 (at 200 THz) is near cutoff, and at this point, we find $|g_{\mathrm{Qu}}| = 0.50$. Moving closer to cutoff along the curve of high $|g_{\mathrm{Qu}}|$, we find that $|g_{\mathrm{Qu}}|$ grows, but not significantly: at 185 THz, $|g_{\mathrm{Qu}}| \approx 0.51$. On the other hand, moving far from cutoff, at the edge of Fig. 2, at 240 THz, we find that $|g_{\mathrm{Qu}}|$ decreases to 0.37. Beyond these cutoff behaviors, we additionally notice that the curve of high $|g_{\mathrm{Qu}}|$ always remains above an electron velocity of $v_e = 0.29c$ (corresponding to an electron energy of $E_e = 23$ keV). As we move further away from cutoff, more of the mode is confined

Optics EXPRESS

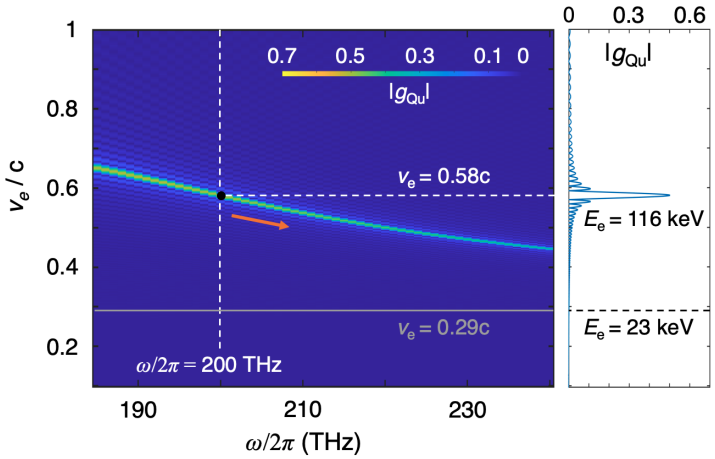

Fig. 2. Coupling coefficient magnitude for the uniform waveguide versus electron velocity (v_e) and mode frequency (ω). g_{Qu} is calculated according to Eq. (1) with an interaction length of L_{int} = 45 μm and an impact parameter of 50 nm. (These parameters are similar to those used in recent experiments [5].) The refractive index of silicon sets the minimum phase velocity of a mode to 0.29c (corresponding to an electron energy of 23 keV).

in the high-index, silicon portion of the waveguide. Therefore, the phase velocity of the mode approaches $c/n_{Si} = 0.29c$, where n_{Si} is the refractive index of silicon. So, for a uniform, silicon waveguide, we expect that we will not be able to achieve velocity matching for electron velocities <0.29c (corresponding to electron energies E_e<23 keV). Additionally, we should note that as we approach these low energies, we expect the interaction to become weaker and weaker as the mode becomes more confined within the waveguide. Indeed, we simulated our uniform waveguide at 400 THz, with the velocity-matched electron velocity of 0.33c (E_e = 30 keV). Here, with most of the mode confined in the silicon, we find $|g_{Qu}| = 0.10$. (We should note that 400 THz was only used here for illustrative purposes; 400 THz is an unrealistic frequency for a silicon waveguide due to linear absorption.)

3. Free electrons coupling to subwavelength grating (SWG) waveguides

To extend electron-mode coupling to lower energy electrons, we explore periodic waveguides. Periodic waveguides, including photonic crystal waveguides [22] and dielectric grating waveguides [23], among other examples, have been used in a wide range of photonics applications, from quantum emitters [24] to distributed feedback lasers [25]. Here, we will focus on periodic waveguides with subwavelength-scale modulation [26]. Specifically, we will explore so-called subwavelength grating (SWG) waveguides.

SWG waveguides resemble uniform waveguides but with periodic changes to the refractive index in the longitudinal direction. These periodic changes occur with periodicity $\Lambda<\lambda/2n_{eff}$, where λ is the free-space wavelength of the guided light, and n_{eff} is the effective refractive index. This effective index is defined such that fundamental component of the propagation constant, k_0, associated with a waveguide mode (at free-space wavelength λ) is given by $k_0 = 2\pi n_{eff}/\lambda$. With modulation at this scale, that is, with $\Lambda<\lambda/2n_{eff}$, guided light (at λ) cannot be diffracted from the waveguide, and low-loss, guided modes can exist [26]. Indeed, SWG waveguides can be approximated as uniform waveguides with anisotropic refractive indices given by effective medium theory [27], and SWG waveguides in SOI platforms have been demonstrated with exceptionally low propagation losses of ≈ 2 dB/cm [26,28]. (For reference, typical foundry-made uniform SOI waveguides exhibit propagation losses in the range of 1-2 dB/cm [29].)

Optics EXPRESS

The coupling of a free electron to an SWG waveguide is illustrated in Fig. 3(a). The SWG waveguide under consideration looks just like our uniform waveguide but with sections of the silicon removed and replaced by air. The waveguide has a periodicity (in the longitudinal, z-direction) of $\Lambda = 300$ nm, and it has a duty cycle of 50%; each period of the guide consists of an 150-nm long stretch of silicon followed by an 150-nm long stretch of air. (We also note that for the waveguide under consideration, at 200 THz, 300 nm $< \lambda/2n_{\text{eff}} \approx 475$ nm; this periodicity is common for SWGs in the communications bands around 1500 nm [28].) In Fig. 3(b), we illustrate a cross-section of the waveguide; the particular SWG under consideration has a height of 450 nm and a width of 550 nm. Overlaid on the cross-section, we also plot the intensity of the fundamental TM-like mode of this waveguide. Note that the intensity distribution is less confined in the SWG waveguide than in the uniform waveguide; since the SWG waveguide consists of air and silicon, we expect it to support modes that are less confined than those in the uniform waveguide. We should additionally note that the SWG waveguide cross-section was chosen such that the cutoff of the fundamental TM-like mode of this waveguide occurs near 200 THz. The fundamental TM-like mode is again studied due to its strong z-directed electric field at the position of the electron; see plot in Fig. 3(d).

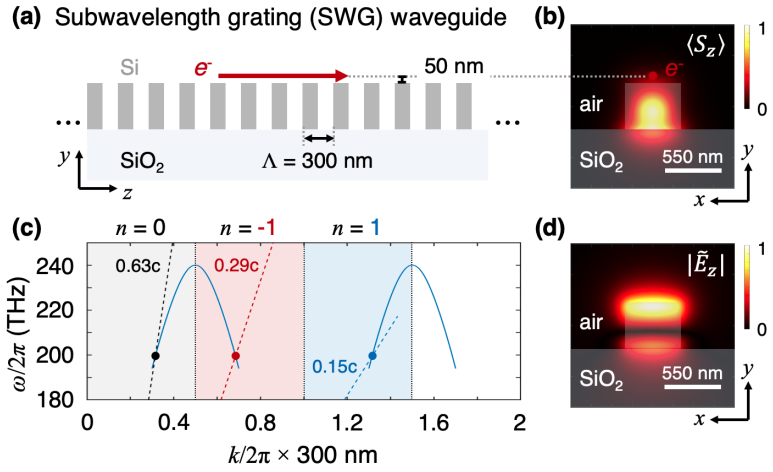

Fig. 3. Free-electron-photon coupling with a periodically modulated, subwavelength grating waveguide. (a) Illustration (side view) of the SWG waveguide, including the propagating free-electron (50 nm above the waveguide). The SWG waveguide has a periodicity of 300 nm with 50% duty cycle. (b) The time-average Poynting vector in the z-direction (i.e., the intensity) of the fundamental TM-like mode (normalized). (c) Dispersion diagram showing that the fundamental TM-like mode consists of different spatial harmonics that can match to different electron velocities; note that the $n = 0$ zone (the first Brillouin zone) is shaded gray, the $n = -1$ zone is shaded red, and the $n = 1$ zone is shaded blue. (d) Longitudinal (z-directed) electric field distribution of the fundamental TM-like mode in the SWG waveguide (normalized). The profiles in (b) and (d) are midway through an air region of the SWG waveguide.

Before discussing electron coupling to the SWG waveguide, we should mention that since our waveguides now vary in the z-direction, in this section we use 3D eigenfrequency simulations. Prior to these simulations, we first approximate the behavior of our SWG waveguides by modeling them via effective medium theory. Specifically, we approximate our SWG waveguides as uniform waveguides with anisotropic refractive indices, and we perform 2D modal analysis on these uniform waveguides. This modal analysis gives us the approximate dispersion of the modes of our SWG waveguides, and using this dispersion as a guide, we perform complete, 3D eigenfrequency

Optics EXPRESS

simulations of the real SWG structures. We should note that each point on our dispersion curve is carefully investigated to ensure lossless behavior (i.e., real frequencies). As before, all simulations are performed in COMSOL.

The periodic, SWG waveguide enables the coupling of low-energy electrons to modes via spatial harmonics. To understand this, let us consider a mode in our periodic, SWG waveguide. According to Floquet's theorem, the complex, z-directed electric field associated with this mode can be expressed as $\tilde{E}_z(x, y, z) = F(x, y, z)e^{-jk_0 z}$ where $F(x, y, z)$ is a periodic function in z, with period Λ. The periodic function $F(x, y, z)$ can be expressed as a sum of harmonics, $F(x, y, z) = \sum_{n=-\infty}^{\infty} f_n(x, y)e^{-j2\pi nz/\Lambda}$, where n represents the order of the harmonic, and $f_n(x, y)$ represents the Fourier series coefficient for the nth harmonic. Plugging this sum into the expression for $\tilde{E}_z(x, y, z)$, we find:

$$\tilde{E}_z(x, y, z) = \sum_{n=-\infty}^{\infty} f_n(x, y)e^{-j2\pi nz/\Lambda}e^{-jk_0 z} = \sum_{n=-\infty}^{\infty} f_n(x, y)e^{-jk_n z}, \tag{2}$$

where $k_n = k_0 + n(2\pi/\Lambda)$. The real, z-directed electric field becomes $E_z(x, y, z, t) = \mathrm{Re}\{\sum_{n=-\infty}^{\infty} f_n(x, y)e^{j(\omega t - k_n z)}\}$. So, the electric field is composed of a superposition of spatial harmonics, with each complex spatial harmonic given by $f_n e^{j(\omega t - k_n z)}$, and k_0 corresponding to the propagation constant of the fundamental spatial harmonic. Importantly, we should note that these spatial harmonics can have low phase velocities; as n grows, the phase velocity of the nth harmonic, $v_{ph,n} = \omega/(k_0 + 2\pi n/\Lambda)$, becomes small. These slow spatial harmonics can velocity match with low-energy, slow electrons. When velocity matched, the electrons can exchange energy with the slow spatial harmonics and, accordingly, with the entire waveguide mode. This basic idea is foundational to numerous vacuum electronic devices, including traveling-wave tubes, backward-wave oscillators, and Smith-Purcell-based radiation sources [30–32].

We can visualize the coupling of low-energy electrons to our SWG waveguide with a dispersion diagram, as illustrated in Fig. 3(c). First, we notice that, as is well known, the dispersion diagram is periodic, with period $2\pi/\Lambda$. Since each mode is composed of spatial harmonics with propagation constants k_n, each ω point in the diagram is associated with propagation constants k_0, $k_1 = k_0 + 2\pi/\Lambda$, $k_2 = k_0 + 4\pi/\Lambda$, etc. Specifically, in Fig. 3(c), we consider a mode at 199.5 THz. This mode has a fundamental spatial harmonic of $k_0 = 0.32 \times (2\pi/\Lambda)$, as shown by the black dot. From Fig. 3(c), we see that the fundamental spatial harmonic intersects with a beam line corresponding to $v_e = 0.63c$ ($E_e = 147$ keV). Furthermore, this mode has its first ($n = 1$) spatial harmonic at a propagation constant $k_1 = (0.32 + 1) \times (2\pi/\Lambda)$, as shown by the blue dot. The first spatial harmonic intersects with a beam line corresponding to $v_e = 0.15c$ ($E_e = 6$ keV). Therefore, an electron with an energy of 147 keV or 6 keV energy could couple to the fundamental or first spatial harmonics, respectively; and this coupling would result in an energy exchange with the mode.

There is one further coupling point shown in Fig. 3(c) that is worth consideration, the point associated with the $n = -1$ harmonic. In Fig. 3(c), we see that a beam line corresponding to $v_e = 0.29c$ ($E_e = 23$ keV) also intersects the dispersion curve at a frequency of 199.5 THz, as shown by the red dot. Inspection of this point indicates that it corresponds to the $n = -1$ harmonic of the mode. The $n = -1$ harmonic should have a propagation constant $k_{-1} = (0.32 - 1) \times (2\pi/\Lambda)$, exactly -1 times the propagation constant at the red point. So, this coupling point corresponds to the $n = -1$ harmonic of the *backwards* propagating version of the mode under consideration at 199.5 THz. (Each mode of the SWG waveguide can be thought of as having a forwards and backwards propagating version.)

To quantify the strength of the coupling between the electron and the SWG-waveguide mode, we plot $|g_{\mathrm{Qu}}|$ for the fundamental TM-like mode in Fig. 4, as we did for our uniform waveguide in Fig. 2. For larger electron velocities, we observe behavior similar to that of the uniform waveguide: the electron couples to the fundamental harmonic and exhibits a large $|g_{\mathrm{Qu}}|$. The

Optics EXPRESS

black dot in Fig. 4 corresponds to the black dot in Fig. 3(c), and we find that at 199.5 THz, an electron with E_e = 147 keV shows $|g_{Qu}|$ = 0.46. As the electron velocity decreases, the behaviors shift. Eventually, as the velocity continues to decrease, the beam line no longer intersects with the fundamental harmonic, and it begins hitting the $n = -1$ harmonic. In this regime, we see the velocity-matching frequency begins to decrease with decreasing velocity, and we hit the red point Fig. 4, corresponding to the intersection at the red point in Fig. 3(c). Here, we find that at 199.5 THz, an electron with E_e = 23 keV has $|g_{Qu}|$ = 0.23. We should emphasize that 23-keV electrons are easily achievable in SEMs, and the coupling coefficient here is comparable in magnitude to the coupling at 147 keV. We should also note that recent experiments with free-electron-photon coupling in TEMs have used a similar impact parameter (≈50 nm) and interaction length ($L_{int} \approx 40$ μm) and found comparable coupling coefficients with 120-keV electrons [5]. Finally, as we continue to decrease the electron velocity, we find coupling with the $n = 1$ harmonic at the blue point, and we also see coupling to the $n = -2$ harmonic.

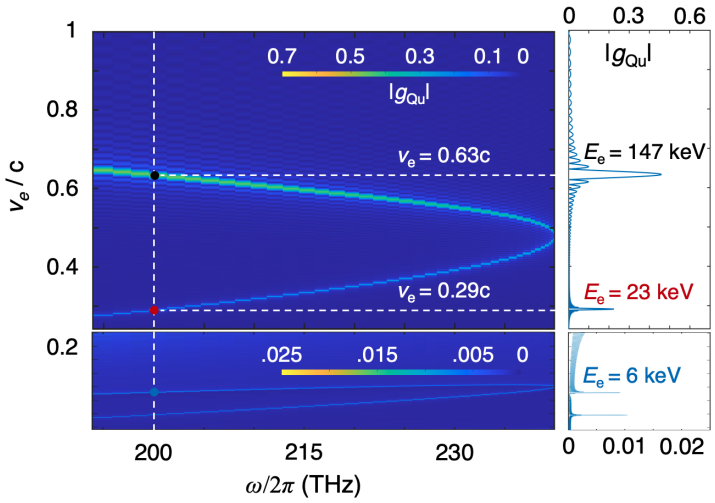

Fig. 4. Coupling coefficient magnitude for the SWG waveguide versus electron velocity (v_e) and mode frequency (ω). As in Fig. 2, g_{Qu} is calculated according to Eq. (1) with an interaction length of L_{int} = 45 μm and an impact parameter of 50 nm. We should note that in the bottom right panel, $|g_{Qu}|$ appears to have a "background" that decreases with decreasing v_e; this background follows from the slowly decaying tail of the sinc-like curves associated with strong matching points at higher electron velocities.

Looking at the results in Fig. 3 and Fig. 4, we can draw several conclusions. Firstly, we notice that as we couple to higher spatial harmonics, the coupling strength decreases. This is exactly what we should expect. Higher harmonics have larger k_n values. These larger k_n values mean that the transverse propagation constants, which are imaginary for the waveguide modes, must also be large. In other words, the large k_n values mean the higher spatial harmonics are more confined to the waveguide core and are weaker at the position of the electron. Additionally, we notice that the $n = -1$ harmonic exhibits the largest coupling. This is also an expected observation. It is well-known that the $n = -1$ harmonic in periodic waveguide structures is typically the strongest harmonic (excluding the fundamental) [33]. Finally, we can make one other intriguing observation: the $n = -1$ harmonic is *backwards propagating*. This was noted previously and is easily seen in Fig. 3(c): the group velocity at the red intersection point is negative. We will explore this point further in the subsequent section.

Beyond these conclusions, we should make several final notes regarding loss. As mentioned, SWG waveguides in similar material platforms have been demonstrated with low propagation

Optics EXPRESS

losses of ≈ 2 dB/cm [26,28]. However, it may seem concerning that our waveguide designs operate relatively close to cutoff, where a less confined mode might experience greater propagation losses. To alleviate this concern, we make two notes. First, we note that uniform waveguides have been demonstrated to operate with a similar proximity to cutoff with minimal additional loss (typically, ~ 1 dB/cm) [34]; additionally, SWG waveguides and components with similar mode confinement (i.e., effective refractive indices) have also been demonstrated with low loss [35]. Second, we note that even if our waveguides experience moderate loss due to fabrication imperfections or near-cutoff operation, the interaction lengths under consideration are sufficiently short that loss should minimally affect performance. For instance, even with a very conservative estimate of 6 dB/cm loss, over an interaction length of 45 μm (as considered here), mode power in our waveguides would only be attenuated by ~ 0.6%.

Before proceeding to the next section, we should briefly summarize our results so far. Here, we have seen that periodic, SWG waveguides should enable electron-mode coupling with low-energy electrons. This coupling should be comparable in strength to that experimentally demonstrated with high-energy electrons, and these periodic waveguides may also allow coupling to interesting modes, including backwards propagating ones. Furthermore, we should note that, beyond the free-electron-photon interaction applications that we have stressed thus far, these waveguides could also find applications in dielectric laser accelerators (DLAs) [36]. DLAs similarly involve velocity matching electrons with light waves, and these periodic waveguides may be useful for developing DLAs with co-propagating electrons and driving light [37,38].

4. Time-domain particle-in-cell simulations

Our results from Section 3 show that periodic, SWG waveguides can enable electron-mode coupling for low-energy electrons. However, the simulations in Section 3 only examine the behavior of a single mode; they do not tell us if higher-order mode coupling is a problem [21]. To gain more insight, in this section we study our SWG waveguide with time-domain, particle-in-cell (PIC) simulations. (For our PIC simulations, we use CST.) We should note that the PIC simulations account for the complete classical interaction of the electron with the field: the simulations include the impact of electric and magnetic fields on a passing electron, as well as the radiation produced by the electron.

We perform time-domain, PIC simulations for two velocity-matched electron velocities, $0.63c$ and $0.29c$, in the SWG waveguide. These velocities correspond to the black and red points, respectively, in Fig. 3(c) and Fig. 4. In our PIC solver, an electron passes above our SWG waveguide at an impact parameter of 50 nm (as considered in the previous sections). The electron is defined as a Gaussian-shaped pulse of macroparticles. Here, since we are considering a single electron, these macroparticles represent a fraction of the electron charge. Specifically, for our simulations, a Gaussian-shaped electron pulse with a 6σ width of 400 nm is used, where σ is the standard deviation of the Gaussian profile. (So, ≈99.7% of the electron charge is contained in a 400-nm length.) This electron pulse width was chosen to be short enough such that nearly all (≈97.5%) of the electron charge is contained within one 300-nm period of the waveguide; at the same time, the pulse width was made long enough such that our PIC simulations smoothly converged. Additionally, we should note that due to machine memory constraints, our total simulation length was limited to 60 periods (18 μm) of the SWG waveguide.

The results of our simulations at $v_e = 0.63c$ (E_e = 147 keV) are displayed in Fig. 5. We should emphasize that the electron pulses are injected into our simulations without any electromagnetic power present in the adjacent waveguide. In Fig. 5(a), we plot the normalized z-component of the Poynting vector at t = 70 fs, corresponding to the time when the electron has traveled 13.2 μm over the waveguide. (t = 0 fs corresponds to when the electron begins to traverse the waveguide.) (A movie associated with Fig. 5(a) is provided as supplementary material in Visualization 1.) The electron is clearly exciting modes in the waveguide, and in Fig. 5(b) we

Optics EXPRESS

show a calculation of the z-directed power carried by these modes. Specifically, we plot the total z-directed electromagnetic power traversing the xy-plane at $z = 14$ μm (that is, the integral of S_z over the xy-plane at this position). The power clearly consists of two parts. First, there is a part associated with the near field carried locally by the electron. This is shaded in gray and labeled "beam". Second, after the electron passes the plane at $z = 14$ μm, we observe further power. This is power that has been coupled into the waveguide, and we label this "mode". We should note that we are plotting instantaneous power, so we expect oscillations at twice the frequency of the associated electromagnetic wave (since power can be related to the square of the field). In the inset of Fig. 5(b), we plot the spectrum of the power displayed in Fig. 5(b). We see a clear and prominent peak at a frequency of 397 THz = 2 × 198.5 THz. This peak corresponds to the expected, velocity-matched coupling point of 199.5 THz that we found in Section 3. See the black dot in Fig. 4. (We should note that the 1-THz frequency deviation may be explained by the phase velocity used in the PIC simulations; this phase velocity was rounded at the third significant digit.) Finally, we should note that the peak at 397 THz shows a full-width-at-half-maximum (FWHM) bandwidth of 26.6 THz.

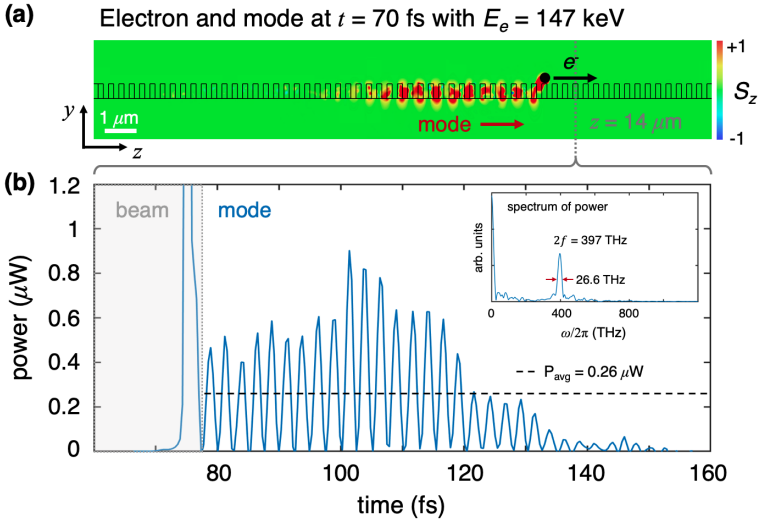

Fig. 5. PIC simulation results for the SWG waveguide with a fast electron, $v_e = 0.63c$. (a) Instantaneous, z-directed power density (S_z) visualized in the yz-plane (side view). S_z is normalized, and as considered previously, the electron is moving above the waveguide with a 50-nm impact parameter. Since S_z>0 (red), the mode is traveling forwards, in the same direction as the electron. (b) Instantaneous power versus time passing through the plane at $z = 14$ μm. The dashed black line shows the average power in the time window $t = 76$ fs to 133 fs. The inset shows the Fourier transform of this power and exhibits a notable peak at ≈397 THz, twice the frequency of the mode.

The results of our simulations at $v_e = 0.29c$ ($E_e = 23$ keV) are shown in Fig. 6. Figure 6 is arranged just like Fig. 5, and in Fig. 6(a), we plot the z-component of the Poynting vector at $t = 140$ fs (corresponding to the time when the electron has traveled 12.2 μm over the waveguide). (A movie associated with Fig. 6(a) is provided as supplementary material in Visualization 2.) The electron is clearly exciting radiation in the waveguide, and notably, this radiation is flowing backwards; since S_z is negative (blue), the power flow is in the negative z-direction. In Fig. 6(b) we include the z-directed power passing the plane at $z = 2.9$ μm. Looking at the power carried in the waveguide (again labeled "mode" in the figure), we notice that this power appears as soon as the electron passes this plane and until $t \approx 349$ fs. (We should note that the electron leaves the

Optics EXPRESS

simulation at t = 207 fs; 349 fs is equal to 207 fs plus the time it takes for the backwards traveling mode to move from the end of the simulation domain at 18 μm to the detection plane at 2.9 μm.) We should again emphasize that this power is negative, so it corresponds to power flowing backwards. In other words, the electron-waveguide system is operating like a backward-wave oscillator [30]. We should stress that this is in exact agreement with our analysis from the preceding section, in Fig. 4. This velocity-matching point corresponds to the $n = -1$ harmonic and the red point in Fig. 4, where the group velocity is negative.

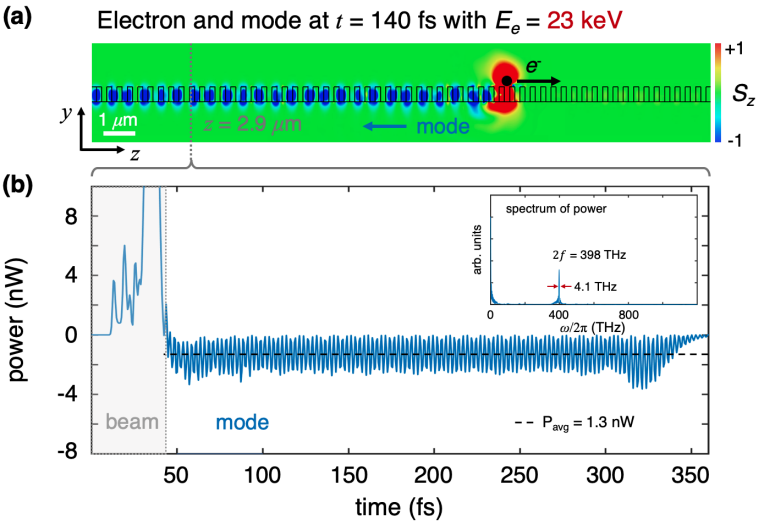

Fig. 6. PIC simulation results for the SWG waveguide with a slow electron, $v_e = 0.29c$. (a) Instantaneous, z-directed power density (S_z), visualized in the yz-plane (side view). S_z is normalized, and the electron is 50 nm above the waveguide. Since S_z<0 (blue), the mode is traveling backwards, in the opposite direction as the electron. (b) Instantaneous power versus time passing through the plane at z = 2.9 μm. The dashed black line shows the average power in the time window t = 45 fs to 358 fs. The inset shows the Fourier transform of this power and exhibits a notable peak at ≈398 THz, twice the frequency of the mode.

In the inset of Fig. 6(b) we plot the spectrum of the instantaneous power flow. The spectrum shows a clear peak at 398 THz = 2 × 199 THz. The peak at 398 THz corresponds to double the frequency of the expected fundamental TM-like mode, that is 199 THz (with 0.5-THz deviation). Additionally, we should note that the FWHM bandwidth of the peak at 398 THz is only 4.1 THz, significantly smaller than that exhibited for the fast-electron coupling, shown in Fig. 5(b). This is to be expected if we consider the dispersion diagram plotted in Fig. 3(c). The fast electron couples to a forwards-traveling mode (see black dot in Fig. 3(c)); so, the the beam line crosses the mode dispersion at a shallow angle, that is, these two lines are close to parallel at their crossing. This leads to a large region of *near* velocity matching. On the other hand, the slow electron couples to a backwards-traveling mode (see red dot in Fig. 3(c)), so the beam line crosses the mode dispersion at a very steep angle; these two lines are close to orthogonal at their crossing. This leads to a small velocity-matching region and a narrow coupling bandwidth.

Thus far we have discussed qualitative agreement between our time-domain simulations and our frequency-domain simulations from Section 3. We can compare these simulations quantitatively by examining the total energy coupled from the electron into the waveguide. Specifically, if we integrate over the power given in Fig. 5(b) and Fig. 6(b), we find that the fast electron ($v_e = 0.63c$) couples 94 meV and the slow electron ($v_e = 0.29c$) couples 2.5 meV into the waveguide over an interaction length of 14 μm and 15.1 μm, respectively. (The interaction length for the fast

Optics EXPRESS

electron and forward wave corresponds to the distance from $z = 0$ to the detection plane at $z = 14$ μm, and the interaction length for the slow electron and backward wave is the distance from the detection plane at $z = 2.9$ μm to the end of the simulation domain at $z = 18$ μm.) Recalling that $|g_{\mathrm{Qu}}|^2$ should equal the number of photons produced in the waveguide per exciting electron, we can convert these energies into $|g_{\mathrm{Qu}}|$ predictions. Additionally, by noting that $|g_{\mathrm{Qu}}|$ scales with the square root of the interaction length, we can scale our $|g_{\mathrm{Qu}}|$ predictions to a 45-μm interaction length, for comparison with the results from Section 3. Putting this all together, we find that our time-domain simulations predict $|g_{\mathrm{Qu,td}}| = 0.34 \times \sqrt{45\ \mu\mathrm{m}/14\ \mu\mathrm{m}} \approx 0.61$ and $|g_{\mathrm{Qu,td}}| = 0.06 \times \sqrt{45\ \mu\mathrm{m}/15.1\ \mu\mathrm{m}} \approx 0.10$ for the fast electron and slow electron, respectively. (The subscript "td" indicates a time-domain prediction.) We can directly compare these coupling coefficient values to the predictions from our frequency-domain calculations in Section 3. Our single-mode, frequency-domain calculations predicted: $|g_{\mathrm{Qu}}| = 0.46$ for the fast electron, and $|g_{\mathrm{Qu}}| = 0.23$ for the slow electron.

The time- and frequency-domain simulations show similar values but with a slight disagreement. One possible resolution to this disagreement could be a group velocity factor. Recent work has suggested that the definition for g_{Qu} should be multiplied by a factor of $\sqrt{1/|1 - v_g/v_e|}$ to account for group velocity effects [17,21]. The group velocity of the forward and backward propagating waves are $v_g = 0.36c$ and $v_g = -0.36c$, respectively. Incorporating the group-velocity factor, our frequency-domain predictions become $|g_{\mathrm{Qu}}| = 0.70$ and $|g_{\mathrm{Qu}}| = 0.15$ for the forward and backward wave, respectively. (The forward and backward wave time-domain predictions were $|g_{\mathrm{Qu,td}}| = 0.61$ and $|g_{\mathrm{Qu,td}}| = 0.10$, respectively.) The group-velocity factor does indeed improve the agreement between the time- and frequency-domain predictions; however, some discrepancy still remains. This discrepancy will be further explored in future work.

5. Conclusion

In this work, we explored periodic, silicon waveguides for enhanced electron-photon interactions at low electron energies. First, we reviewed the basic coupling of free-electrons to electromagnetic modes in an adjacent waveguide. Next, we introduced subwavelength grating (SWG) waveguides as a means to velocity match slow, low-energy electrons with co-propagating electromagnetic modes, and we showed that such waveguides can support large coupling coefficients and unique opportunities for dispersion engineering. Finally, we validated our SWG waveguide designs via time-domain, particle-in-cell simulations. These simulations revealed that SWG waveguides, and periodic waveguides in general, can enable unique behaviors like backward-wave oscillations.

Funding. National Science Foundation (2110556); Air Force Office of Scientific Research (FA9550-21-1-0270).

Acknowledgments. We thank P. D. Keathley, J. W. Simonaitis, S. A. Koppell, M. A. R. Krielaart, and R. S. Kim for helpful discussions.

Disclosures. The authors declare no conflicts of interest.

Data availability. Data underlying the results presented in this paper are not publicly available at this time but may be obtained from the authors upon reasonable request.

References

1. B. Barwick, D. J. Flannigan, and A. H. Zewail, "Photon-induced near-field electron microscopy," Nature **462**(7275), 902–906 (2009).
2. S. T. Park, M. Lin, and A. H. Zewail, "Photon-induced near-field electron microscopy (PINEM): theoretical and experimental," New J. Phys. **12**(12), 123028 (2010).
3. A. Ryabov, J. W. Thurner, D. Nabben, *et al.*, "Attosecond metrology in a continuous-beam transmission electron microscope," Sci. Adv. **6**(46), eabb1393 (2020).
4. D. Nabben, J. Kuttruff, L. Stolz, *et al.*, "Attosecond electron microscopy of sub-cycle optical dynamics," Nature **619**(7968), 63–67 (2023).
5. A. Feist, G. Huang, G. Arend, *et al.*, "Cavity-mediated electron-photon pairs," Science **377**(6607), 777–780 (2022).
6. O. Kfir, "Entanglements of Electrons and Cavity Photons in the Strong-Coupling Regime," Phys. Rev. Lett. **123**(10), 103602 (2019).

Optics EXPRESS

7. A. Konečná, F. Iyikanat, and F. J. G. De Abajo, "Entangling free electrons and optical excitations," Sci. Adv. **8**(47), eabo7853 (2022).
8. G. Baranes, R. Ruimy, A. Gorlach, *et al.*, "Free electrons can induce entanglement between photons," npj Quantum Information **8**(1), 32 (2022).
9. G. Baranes, S. Even-Haim, R. Ruimy, *et al.*, "Free-electron interactions with photonic GKP states: Universal control and quantum error correction," Phys. Rev. Res. **5**(4), 043271 (2023).
10. T. P. Rasmussen, A. R. Echarri, J. D. Cox, *et al.*, "Generation of entangled waveguided photon pairs by free electrons," Sci. Adv. **10**(12), eadn6312 (2024).
11. R. Dahan, S. Nehemia, M. Shentcis, *et al.*, "Resonant phase-matching between a light wave and a free-electron wavefunction," Nat. Phys. **16**(11), 1123–1131 (2020).
12. O. Kfir, H. Lourenço-Martins, G. Storeck, *et al.*, "Controlling free electrons with optical whispering-gallery modes," Nature **582**(7810), 46–49 (2020).
13. R. Shiloh, T. Chlouba, and P. Hommelhoff, "Quantum-coherent light-electron interaction in a scanning electron microscope," Phys. Rev. Lett. **128**(23), 235301 (2022).
14. Y. Yang, A. Massuda, C. Roques-Carmes, *et al.*, "Maximal spontaneous photon emission and energy loss from free electrons," Nat. Phys. **14**(9), 894–899 (2018).
15. A. Karnieli and S. Fan, "Jaynes-cummings interaction between low-energy free electrons and cavity photons," Sci. Adv. **9**(22), eadh2425 (2023).
16. A. P. Synanidis, P. A. D. Gonçalves, C. Ropers, *et al.*, "Quantum effects in the interaction of low-energy electrons with light," Sci. Adv. **10**(25), eadp4096 (2024).
17. A. Karnieli, C. Roques-Carmes, N. Rivera, *et al.*, "Strong coupling and single-photon nonlinearity in free-electron quantum optics," ACS Photonics **11**(8), 3401–3411 (2024).
18. Z. Zhao, "Upper bound for the quantum coupling between free electrons and photons," arXiv (2024).
19. L. Chrostowski and M. Hochberg, *Silicon Photonics Design: From Devices to Systems* (Cambridge University Press, 2015).
20. R. W. Boyd, *Nonlinear Optics* (Academic Press, 2020).
21. G. Huang, N. J. Engelsen, O. Kfir, *et al.*, "Electron-photon quantum state heralding using photonic integrated circuits," PRX Quantum **4**(2), 020351 (2023).
22. J. D. Joannopoulos, S. G. Johnson, J. N. Winn, *et al.*, *Photonic Crystals: Molding the Flow of Light* (Princeton University Press, 2008).
23. T. Itoh, "Application of gratings in a dielectric waveguide for leaky-wave antennas and band-reject filters (short papers)," IEEE Trans. Microwave Theory Tech. **25**(12), 1134–1138 (1977).
24. M. Arcari, I. Söllner, A. Javadi, *et al.*, "Near-Unity Coupling Efficiency of a Quantum Emitter to a Photonic Crystal Waveguide," Phys. Rev. Lett. **113**(9), 093603 (2014).
25. S. Wang, "Principles of distributed feedback and distributed Bragg-reflector lasers," IEEE J. Quantum Electron. **10**(4), 413–427 (1974).
26. P. Cheben, R. Halir, J. H. Schmid, *et al.*, "Subwavelength integrated photonics," Nature **560**(7720), 565–572 (2018).
27. S. Rytov, "Electromagnetic properties of a finely stratified medium," JETP **2**, 466–475 (1956).
28. P. J. Bock, P. Cheben, J. H. Schmid, *et al.*, "Subwavelength grating periodic structures in silicon-on-insulator: a new type of microphotonic waveguide," Opt. Express **18**(19), 20251–20262 (2010).
29. S. Y. Siew, B. Li, F. Gao, *et al.*, "Review of silicon photonics technology and platform development," J. Lightwave Technol. **39**(13), 4374–4389 (2021).
30. S. E. Tsimring and J. Love, *Electron Beams and Microwave Vacuum Electronics* (Wiley, 2006).
31. L. Schächter, *Beam-Wave Interaction in Periodic and Quasi-Periodic Structures* (Springer, 2011).
32. P. M. Van den Berg, "Smith-purcell radiation from a line charge moving parallel to a reflection grating," J. Opt. Soc. Am. **63**(6), 689–698 (1973).
33. S. T. Peng, T. Tamir, and H. L. Bertoni, "Theory of Periodic Dielect Waveguides," IEEE Trans. Microwave Theory Tech. **23**(1), 123–133 (1975).
34. Y. A. Vlasov and S. J. McNab, "Losses in single-mode silicon-on-insulator strip waveguides and bends," Opt. Express **12**(8), 1622–1631 (2004).
35. V. Donzella, A. Sherwali, J. Flueckiger, *et al.*, "Sub-wavelength grating components for integrated optics applications on soi chips," Opt. Express **22**(17), 21037–21050 (2014).
36. R. J. England, R. J. Noble, K. Bane, *et al.*, "Dielectric laser accelerators," Rev. Mod. Phys. **86**(4), 1337–1389 (2014).
37. Z. Zhao, T. W. Hughes, S. Tan, *et al.*, "Design of a tapered slot waveguide dielectric laser accelerator for sub-relativistic electrons," Opt. Express **26**(18), 22801–22815 (2018).
38. Y. D'Mello, R. Dahan, S. Bernal, *et al.*, "Efficient coupling between free electrons and the supermode of a silicon slot waveguide," Opt. Express **31**(12), 19443–19452 (2023).